

# INVESTIGATION OF AERODYNAMICS OF RIGID FLAPPING WINGS FOR MAV APPLICATIONS: CFD VALIDATION

Ria Malhan \*

Vinod K. Lakshminarayan †

James Baeder ‡

Inderjit Chopra §

Alfred Gessow Rotorcraft Center  
Department of Aerospace Engineering  
University of Maryland  
College Park, MD 20742.

## ABSTRACT

In this work, an existing compressible Reynolds-Averaged Navier-Stokes (RANS) solver is extended to investigate the aerodynamics of flapping wing MAVs, with the ultimate goal of developing a predictive tool to refine the design of such MAVs. The primary objective of the current work is to carefully validate the computational methodology against prior experimental and computational results. The numerical predictions are first validated in 2D, at high ( $\sim 10^6$ ) as well as low ( $\sim 15,000$ ) Reynolds numbers and a good correlation is achieved with prior work. For pure plunge motion, propulsive thrust is produced only when the leading edge vortex remains ahead of the position of maximum thickness of the airfoil. On the other hand, for a combined pitch and plunge motion, the chordwise force can be more easily vectored by tailoring the combination of the instantaneous effective angle of attack and pitch angle. Next, the numerical predictions are validated in 3D flow environment for two different cases: (1) a low aspect ratio flat plate with heaving and pitching motion and (2) a NACA0005 wing with root based flapping motion, which is more representative of natural flyers. A good correlation of the instantaneous forces as well the flow-field data is obtained with prior work for both the cases. It is observed that the flapping kinematics could be optimized to produce the lift and thrust required for application to MAVs. The flowfield is found to be highly three dimensional for the root flap case with the flow dominated by leading edge vortices in the midsection but by the root and tip vortices near the ends of the wing.

## Nomenclature

$a$	Speed of sound, m/s
$AR$	Aspect Ratio
$b$	Span length, m
$c$	Airfoil chord, m
$C_d$	Drag force coefficient
$C_l$	Lift force coefficient
$f$	Flapping frequency, Hz
$h$	Plunge displacement (non dim. by chord)
$h_o$	Plunge amplitude (non dim. by chord)
$k$	Reduced frequency
$M_\infty$	Free stream Mach number, $U_\infty/a$
$Re$	Reynolds number
$U_\infty$	Free stream velocity, m/s

$U_{tip}$	Tip speed, m/s
$\alpha$	Angle of attack
$\gamma_o$	Flapping amplitude, deg
$\gamma$	Flapping angle, deg
$\phi$	Phase difference between pitch and plunge, deg
$\theta$	Pitch angle, deg
$\theta_o$	Fixed pitch angle, deg
$\theta_a$	Pitch amplitude, deg

## Introduction

Micro air vehicles offer a great potential in exploration, communication, surveillance and reconnaissance missions especially in constrained environments. The DARPA (Defense Advanced Research Projects Agency) defined MAVs as flying vehicles having no dimension larger than 15 cm and the gross weight of less than 100 grams. In order to carry out different missions, MAVs should be efficient, maneuverable and capable

\*Graduate Research Assistant, rmalhan@umd.edu

†Research Associate, vinodkl@umd.edu

‡Associate Professor, baeder@eng.umd.edu

§Alfred Gessow Professor, chopra@umd.edu

of hover. Due to their small size, they operate at low Reynolds numbers. They can be classified into three broad categories: fixed wing, rotary wing and bio-inspired flapping wing vehicles. The fixed wing and rotary wing MAVs are scaled down versions of the traditional full scale concepts. Fixed wing MAVs are efficient, however, they lack the ability to hover and thus, they are unsuitable for operations in confined spaces. Rotary wing MAVs are hover capable, however, they have lower efficiency as compared to fixed wing MAVs (Ref. 1). Since MAVs operate in the Reynolds number regime of 10,000-100,000, which is about the same at which large insects and small birds operate, it may be beneficial to take inspiration from natural flyers to learn their flight physics.

There have been a number of experimental studies to understand the aerodynamics of flapping wings. Pure plunging of a wing in free-stream results in an effective angle of attack during both, the up-stroke and down-stroke, which results in a net positive thrust. The directions of lift and thrust are shown in Fig. 1. Knoller and Betz were the first to identify this phenomenon (Refs. 2, 3). Katzmayr experimentally verified this fact in 1922 by measuring the thrust from a stationary wing placed in a sinusoidally oscillating wind stream (Ref. 4). Pitching/plunging airfoils at high Reynolds numbers (on the order of million) were studied in detail while investigating dynamic stall of helicopter blades. The formation of a leading edge vortex due to flow separation was found to have significant effect on the blade aerodynamics. This leads to forces and moments that are very different from static stall values. McCroskey (Ref. 5) and Carr (Ref. 6) provided comprehensive reviews on this topic. While this work can serve as a starting point for investigating flapping wing MAV aerodynamics, the Reynolds number regime is atleast an order to two higher.

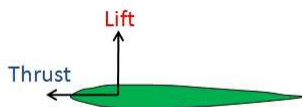


Figure 1: Definition of lift and thrust

At MAV scale Reynolds numbers, experiments have been carried out by Anderson et al. (Ref. 7). It was found that despite the shedding of strong leading edge vortices, the thrust continues to increase with reduced frequency and plunge amplitude. However, these studies were done in a 2D flow environment and may not provide sufficient insight into the flow physics of a flapping wing MAV. Since MAV flapping wings generally have a very low aspect ratio, it may be expected that 3D effects will have an important role to play. In addition, Anderson et al. mainly concentrated on thrust generation due to flapping

wing. For use on an MAV, sufficient vertical lift needs to be generated in addition to the propulsive thrust. Hart et al. (Ref. 8) have experimentally measured the instantaneous lift and drag of a pitching and plunging small aspect ratio flat plate wing. The study also includes PIV measurement of the flow-field at one spanwise location. Even though, this study provides good data for computational validation, it does not provide much insight into the flow physics. Recently, separate experiments have been carried out by Malhan et al. (Ref. 9) and Yuan et al. (Ref. 10) on root based flapping, which closely mimic the kinematics of avian flight. Both these experiments measured instantaneous forces over a flap cycle. In addition, Malhan et al. have shown that it is possible to optimize the kinematics of flapping wings, such that it can be feasible in hover and forward flight. However, neither of these studies performed any flow-field measurement.

Although significant progress has been made in the experimental studies of MAV-scale flapping wings, the fluid physics of the flapping wing MAVs is still not very well understood, mainly because of the challenges faced by experiments. Most importantly, it is extremely difficult to obtain good flow visualization in these experiments. In addition, there are inaccuracies associated with measuring the instantaneous forces.

Computational methods can overcome some of the shortcomings of experiments and help in providing better understanding of the flow physics of flapping wing MAVs. Several computational studies have been done in the past on flapping wings. Two-dimensional Navier Stokes computations of pure plunging airfoils, and airfoils in combined pitch and plunge motions at Reynolds number of the order of 1 million have been carried out by Tuncer et al. (Refs. 11, 12) and Isogai et al. (Ref. 13).

In the Reynolds number regime that is pertinent to the current study, Young et al. (Ref. 14) have simulated the “2D” experiments of Anderson et al. (Ref. 7). However, there has been very limited work on 3D CFD involving flapping wings at this Reynolds number regime. Recently, researchers at University of Michigan, as a part of NATO task group AVT-149 (Ref. 15), have simulated the pitching-plunging flat plate experiments of Hart et al. (Ref. 8) and have obtained reasonable validation with the experimental force measurement. Another recent study by Yuan et al. (Ref. 10) simulated their own root flapping experiments using an incompressible CFD solver and obtained good correlation with the measured forces. They also provided some understanding of the flow physics.

The focus the current work is to extend the limited body of work on 3D flapping wing Navier Stokes simulations and develop computational methodologies to study the performance and flow physics of realistic flapping wing MAVs. Earlier work by Lakshminarayan and

Baeder (Refs. 16–18) demonstrated the capability of using a compressible Reynolds Averaged Navier-Stokes (RANS) solver to study the flow physics of hovering micro-rotors. The aim of this paper is to extend the methodologies developed there to perform 3D flapping wing simulations and carefully validate them against the available experimental and computational data. Prior to validating the methodologies in 3D, validation will be done in 2D for pitching/plunging airfoils operating from high to low Reynolds numbers. Next, two types of motion will be investigated in 3D. Firstly, the entire wing heaving and pitching simulation will be validated against the experimental data of Hart et al. (Ref. 8) and CFD data from the NATO report (Ref. 15). Secondly, the root based flapping calculation will be validated using the results published by Yuan et al. (Ref. 10). Detailed study in understanding the flow physics of flapping wing MAVs will be carried out as a part of future work.

## Numerical Method

Both 2D and 3D simulations of the flapping wing are done using OVERTURNS (Ref. 18), a compressible structured overset RANS solver developed at the University of Maryland. The code solves the compressible RANS equations using the diagonal form of the implicit approximate factorization method developed by Pulliam and Chaussee (Ref. 19) with second order accuracy in time. The inviscid terms are computed using a third-order MUSCL scheme with Roe flux difference splitting and Korens limiter, and the viscous terms are computed using second-order central differencing. When low Mach numbers are involved, time accurate low Mach preconditioning in dual-time scheme described by Buelow et al. (Ref. 20) and Pandya et al. (Ref. 21) is used. Preconditioning is used not only to improve convergence, but also to improve accuracy. Spalart-Allmaras (Ref. 22) turbulence model is employed for RANS closure.

## 2D Code Validation for Pitching and Plunging Airfoils

The code is first validated for pure plunge cases at relatively high Reynolds numbers ( $10^6$ ) against the simulations carried out by Tuncer et al. (Refs. 11, 12). Combined pitch and plunge is then simulated, again at relatively high Reynolds numbers ( $10^5$ ) and results are validated with those of Isogai et al. (Ref. 13). Finally, combined pitch and plunge is examined at MAV-scale Reynolds number regime and validated against numerical predictions carried out by Yuan et al. (Ref. 10). In all the cases, satisfactory correlation is achieved.

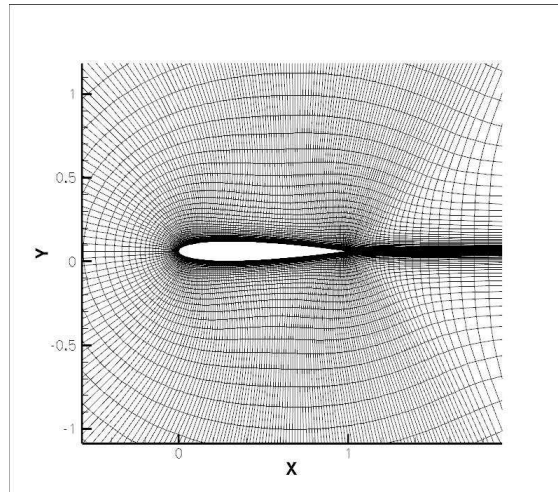


Figure 2: C-grid for NACA 0012

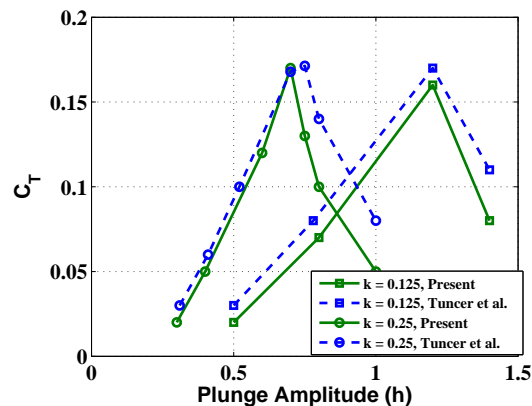


Figure 3: Variation of  $C_T$  with plunge amplitude (pure plunge)

### Pure Plunge ( $M = 0.3$ , $Re = 10^6$ )

First, a flapping NACA0012 airfoil at relatively high Mach number for MAV applications of 0.3, and Reynolds number of  $10^6$ , which was computationally investigated by Tuncer and Platzer (Ref. 12) is considered. The simulation is done using a C-type grid with 327 points in the streamwise and 85 points in the normal direction, see Fig. 2.

The plunge amplitude ( $h$ ) is varied from 0.4 to 1.4 (non-dimensionalized by chord), and reduced frequencies ( $k = 2 \cdot \pi \cdot fc / (2 \cdot U)$ ) of 0.125 and 0.25 are considered. Figure 3 shows thrust as a function of plunge amplitude for both the reduced frequencies. Clearly, a good correlation is observed between the two results. It can be seen that increasing the reduced frequency, increases the thrust produced. Also, for both reduced frequencies, as the plunge amplitude is increased, the mean thrust in-

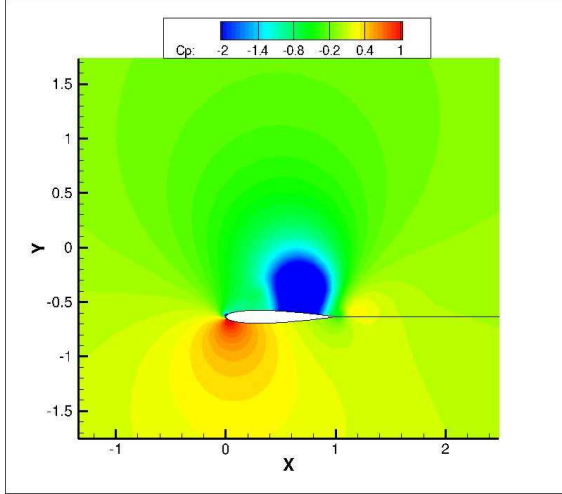


Figure 4:  $C_p$  contour plot for  $k = 0.125$ ,  $h = 1.4$  as airfoil moves downwards (pure plunge)

creases till a certain point and then drops sharply. At smaller plunge amplitudes, an increase in the plunge amplitude creates larger suction pressure at the leading edge, resulting in greater propulsive force. As the plunge amplitude is increased, leading edge vortex is formed over the airfoil. As long as the vortex is ahead of the maximum thickness position, it produces thrust. But, with further increase in plunge amplitude, the leading edge vortex is shed and moves aft towards the trailing edge. The low pressure center of this aft moving vortex creates a force which is vectored in direction of drag, thus decreasing the thrust. This is clearly illustrated in Fig. 4, which shows the contour plot of pressure coefficient over the airfoil as it moves from the middle of the downstroke to the bottom most position, for the case with  $k = 0.125$ ,  $h = 1.4$ . It was observed by Tuncer et al. (Ref. 12) that the shedding of leading edge vortex occurs when  $k \times h$  exceeds 0.175.

#### Pure Plunge: Higher Reduced frequency ( $M = 0.3$ , $Re = 10^6$ )

The second case considered is a high frequency case (Ref. 11) ( $k = 1.0$  and  $1.5$ ), where, the onset of dynamic stall did not have a very drastic effect. Unlike the previous case, a sharp drop in thrust is not seen as plunge amplitude is increased (Fig. 5). This is because the leading edge vortex did not have sufficient time to develop and convect aft of the airfoil due to high frequency plunging motion (Fig. 6). Thus the suction force due to the vortex is always pointed in the thrust direction and we do not see a drop off. The current simulation predicts this behavior correctly.

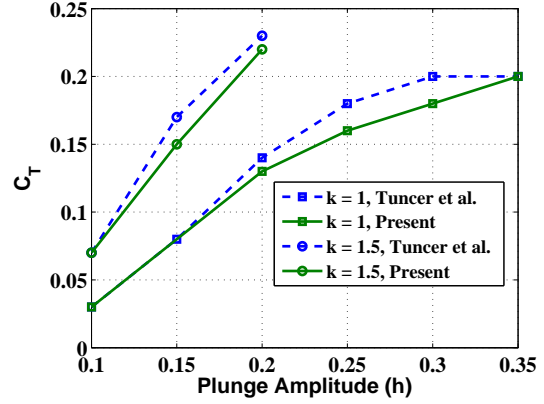


Figure 5: Variation of thrust with frequency for higher reduced frequency (pure plunge)

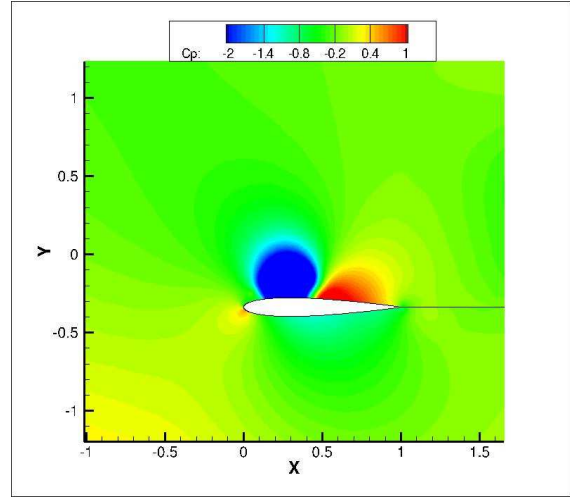


Figure 6:  $C_p$  contour plot for  $k = 1.0$ ,  $h = 0.35$  as airfoil moves downwards (pure plunge)

#### Combined Pitch and Plunge Motions ( $M = 0.3$ , $Re = 10^5$ )

The third case considered is combined pitch and plunge motion. Validation is carried out with the results by Isogai et al. (Ref. 13). The airfoil oscillates in pitch about mid-chord at Mach number of 0.3 and Reynolds number of  $10^5$ . The pitch and plunge motions are given by:  $h = h_0 \cos(kt)$  and  $\alpha = \alpha_0 \cos(kt + \phi)$ .

For the first combined pitch and plunge case, (Case A),  $h_0 = 0.5$  and  $\alpha_0 = 20^\circ$ , results are shown in Fig. 7. The phase difference ( $\phi$ ) between pitch and plunge determines the effective angle of attack. As the frequency is increased, a shift in phase angle is observed at the frequency at which the highest  $C_T$  occurs.

For the second combined pitch and plunge case, (Case B),  $h_0 = 1$ ,  $\alpha_0 = 10^\circ$ , results are presented in Fig. 8.

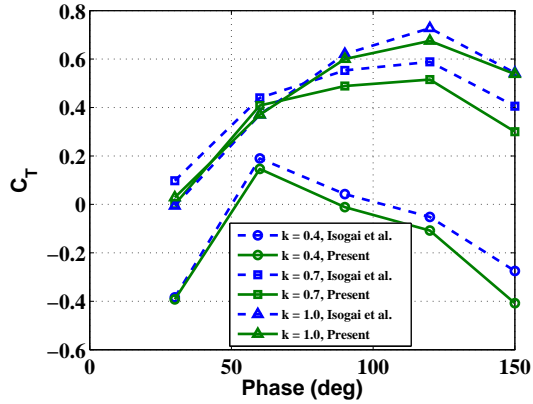


Figure 7: Case A,  $h_0 = 0.5$  and  $\alpha_0 = 20^\circ$  (combined pitch and plunge)

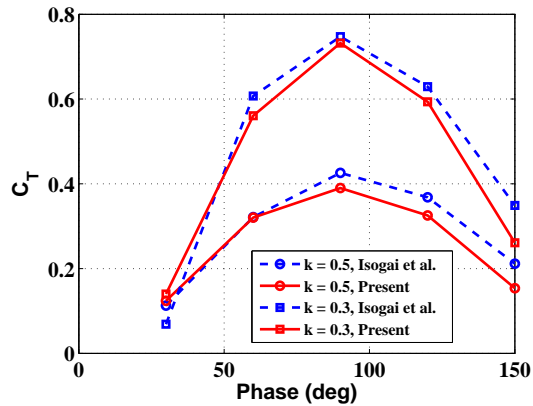


Figure 8: Case B,  $h_0 = 1.0$  and  $\alpha_0 = 10^\circ$  (combined pitch and plunge)

Due to higher plunge amplitudes, large-scale leading edge separation occurs. This separation increases as the frequency is increased and thus, reduces the propulsive thrust. For a phase difference of  $90^\circ$ , the maximum effective angle of attack is reduced and thus stall is avoided. Hence, we see highest thrust for  $\phi = 90^\circ$ . The results from the current simulation correlate well with those by Isogai et al. (Ref. 13) in both the cases.

It should be noted that in case of combined pitch and plunge, the direction in which the chordwise force points is a result of the positioning of the leading edge vortex and also the instantaneous pitch angle. Comparing the average thrust while using combined pitch and plunge motion with that while using pure plunge motion, it is observed that in general, the use of combined mechanism produces higher thrust values. Also, if the phasing between pitch and plunge, and the reduced frequency is tailored correctly, the thrust production can be significantly increased.

### Low Reynolds number case ( $Re = 15,000$ ): Combined Pitch and Plunge

Next, combined pitch and plunge at Reynolds number of 15,000 (based on maximum plunge velocity) is considered, which is more representative of flapping wing MAVs.

Validation of instantaneous forces is carried out with the 2D simulation done by Yuan et al. (Ref. 10). The simulation is done for a pitching and plunging NACA 0005 airfoil. The plunge amplitude is one chord and pitching amplitude is  $40^\circ$ . The airfoil oscillates about the leading edge. The phase difference between the pitch and plunge is  $90^\circ$ . The reduced frequency is 1.6Hz. Yuan et al. used an incompressible solver for their simulation. Since a compressible solver is used in this study, the freestream Mach number is set to 0.05, which is well within the incompressible limits. The instantaneous lift and drag over a plunge cycle from the current simulation is compared

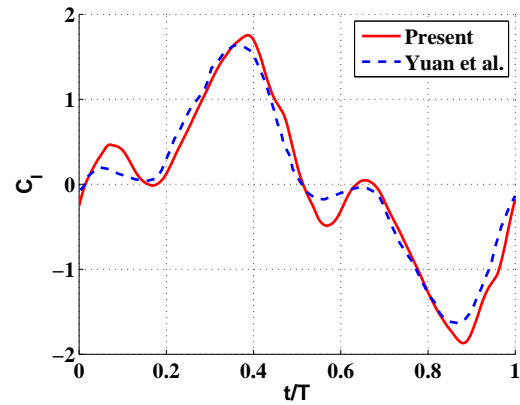


Figure 9:  $C_l$  Variation with time for low Re (combined pitch and plunge)

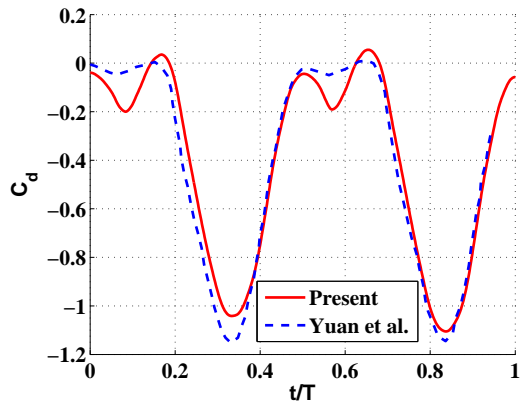


Figure 10:  $C_d$  Variation with time for low Re (combined pitch and plunge)

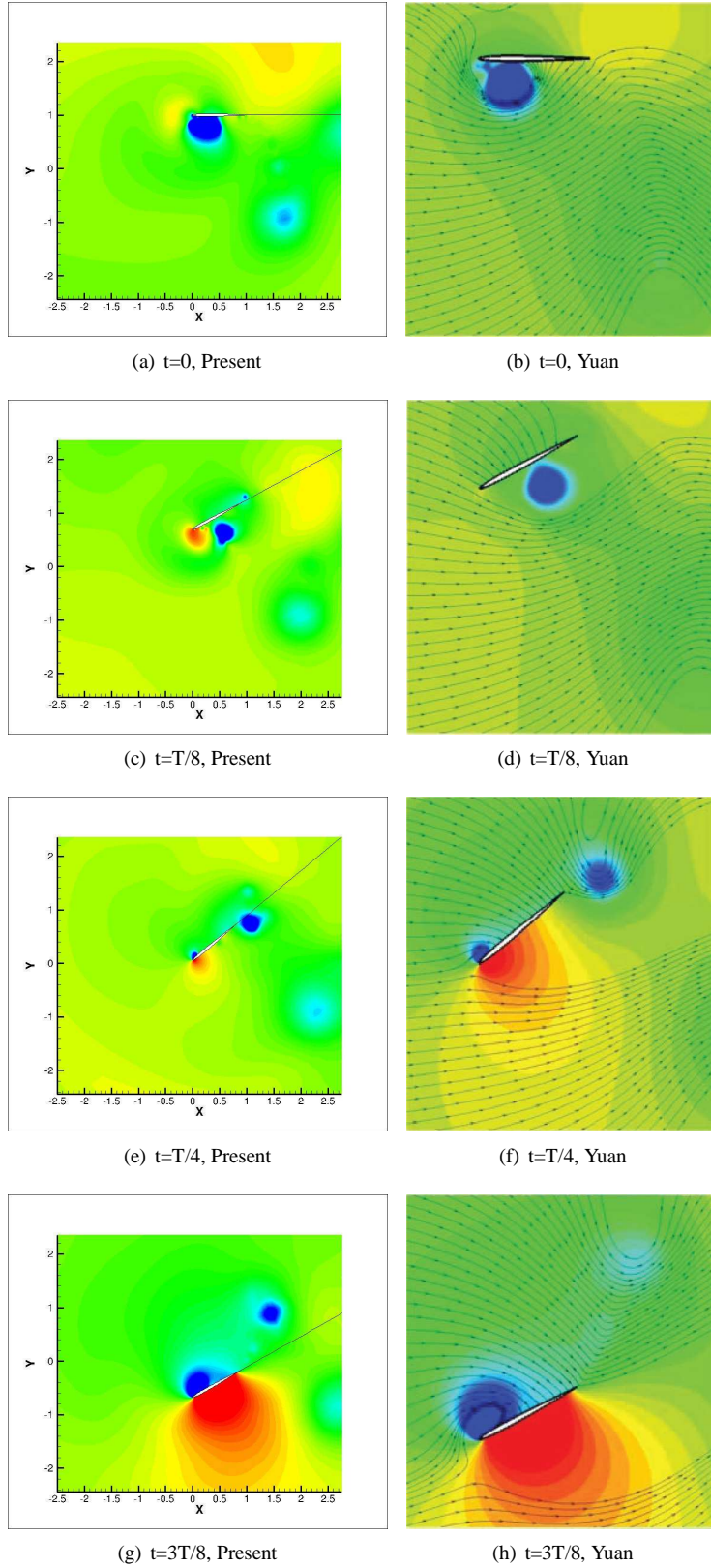


Figure 11: Pressure contours for 2D Simulation at low Re (combined pitch and plunge)

with that from Yuan et al. in Figs. 9 and 10, respectively. Note that,  $t/T = 0$  corresponds to when the airfoil is at the highest plunge position. Clearly, the results agree very well. The average lift is zero because it cancels out in the upstroke and downstroke. On the other hand, positive thrust is produced during both the strokes as a result of the inherent kinematics and therefore, a net thrust is produced over a plunge cycle. The average thrust coefficient predicted by the current simulation is  $-0.40$ . It differs by 18% from the average  $C_d$  of Yuan et al. (Ref. 10). Though the average lift coefficient is zero, the maximum instantaneous lift coefficient reaches a value of 1.75 at  $t/T = 0.4$  when the effective angle of attack seen by the airfoil is  $38^\circ$ . Though statically, the airfoil would have stalled at such high angles, due to the unsteady effects, a large lift coefficient is obtained.

A more detailed comparison of the two CFD results is done by comparing the contours of pressure coefficient, shown in Fig. 11 at different instances in time. Note that the pressure coefficient is obtained by normalizing with respect to the maximum plunge velocity. Again, there is excellent agreement between the results obtained from the two CFD codes, clearly demonstrating the validity of the current methodology. Note that, the present case closely mimics the reference section of the 3D root flapping simulation done later in the paper and some discussion on the pressure contour plot will be done at that point.

### 3D Code Validation for Pitching and Plunging Airfoils

Having obtained good validation for 2D simulation, the next step is to validate the methodology in 3D. Two types of wing motions are considered. The first motion is the

entire wing heaving and pitching. The second type of motion is closer to avian flight with the flapping wing fixed at the root.

#### Flat plate with Aspect Ratio of 2 (Pitching+Plunging)

For the first type of motion, wing heaving and pitching, experiments conducted by Hart et al. (Ref. 8) are simulated. These experiments were done on a flat plate with  $t/c$  of 3.07% at Reynolds number of 40,000 based on chord and free stream velocity. PIV data of the flow velocities at different instants of flapping motion along with the instantaneous lift and drag forces acting on the wing are available. The plunge kinematics is defined by

$$h = h_0 \cos(2 \cdot \pi f \cdot t)$$

and the pitch kinematics is defined by

$$\theta = \theta_a \cos(2 \cdot \pi f \cdot t + \phi) + \theta_o$$

Table 1: Parameters for 3D flat plate wing kinematics.

Case	$h_o$	$f(\text{Hz})$	$\theta_o$	$\theta_a$	$\phi$
1	0.5	2	8	8.45	90
2	0.5	2	8	0	0

Two cases are examined: combined pitch and plunge (Case 1), and pure plunge (Case 2). The parameters for the two cases are shown in Table 1. The reduced frequency is 0.25. These are same as the canonical problems, which are the subject of AVT-149 NATO task group (Ref. 15) and have been studied numerically at University of Michigan. This numerical study was done using an incompressible unstructured RANS solver that uses Menter's SST turbulence model (Ref. 23) for RANS closure. Details on their mesh and time-step sizes are not available.

The present simulation is run on a body-fitted curvilinear C-O type blade mesh with clustering at the blade

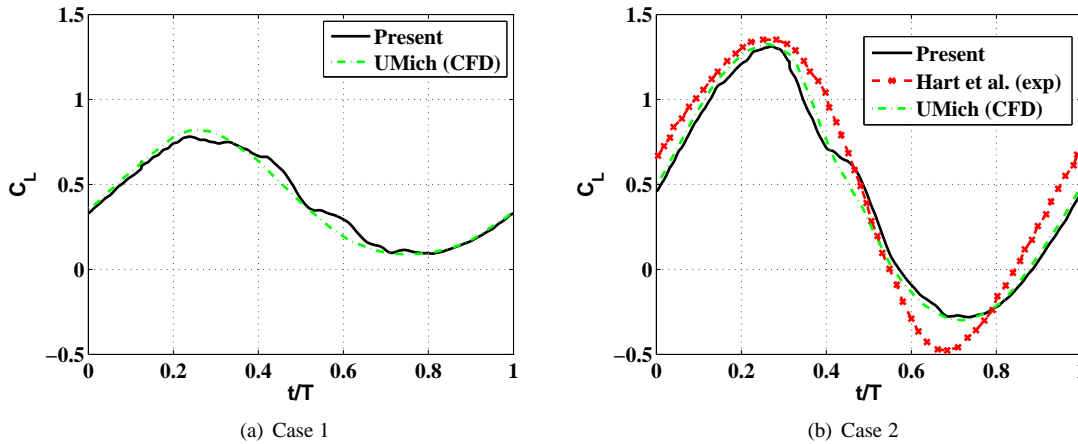


Figure 12:  $C_L$  variation with time for 3D flat plate

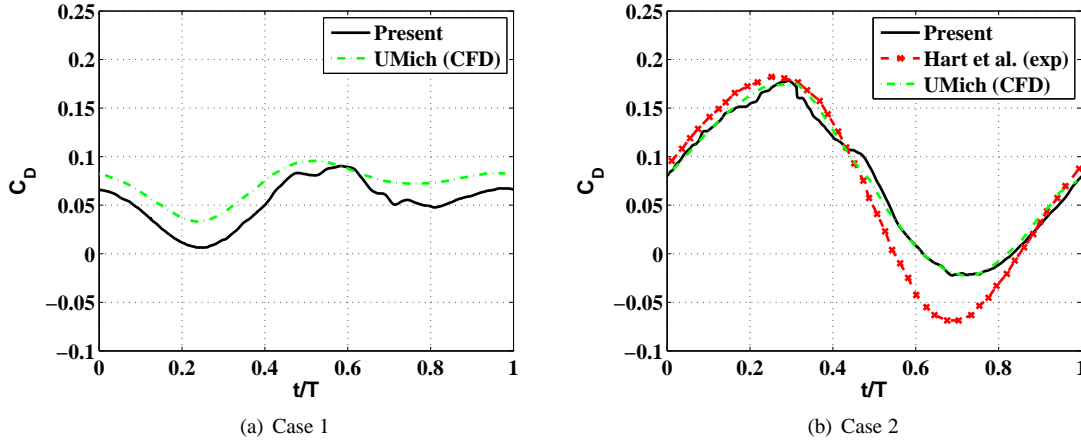


Figure 13:  $C_d$  variation with time for 3D flat plate

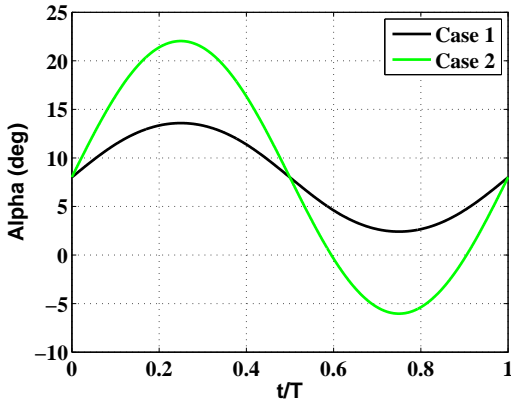


Figure 14: Variation of angle of attack over a flap cycle

tips, leading edge, and trailing edge to capture all the flow structures. The grid has 277 points in wrap around, 109 points in spanwise and 85 points in normal directions. The outer boundary of the mesh extends to 20 chords away from the blade in all directions. Calculations are done using 1440 iterations per cycle and each iteration uses 6 sub-iterations to remove linearization error.

Figure 12 shows the variation of lift coefficient ( $C_L$ ) for case 1 and case 2 over a flap cycle. Figure 13 shows the variation of drag coefficient ( $C_D$ ). The results for case 1 are compared with those from University of Michigan in Ref. 15, since Hart et al. (Ref. 8) have not published the instantaneous values for this case. The figure clearly shows that the current CFD results agree really well with the computational result from Ref. 15 for both cases. When the computational results are compared with the experimental data for case 2, instantaneous lift shows good correlation at all times. The average lift for the two cases differ by 4% and 12%, respectively, from the re-

sults published by University of Michigan in the NATO report (Ref. 15).

Both these cases produce a net lift due to the mean positive pitch angle. The average lift coefficient over a cycle for the cases 1 and 2 from current study are 0.415 and 0.443, respectively. Even though, the mean lift between the two cases differ by only about 6%, the maximum instantaneous lift attained by case 2 is significantly higher compared to that of case 1. This is because of the larger maximum instantaneous effective angles seen by the blade in case 2 as compared to case 1, see Fig. 14. The effective angle is defined here as the angle at quarter chord based on pitch angle and plunge velocity. Also, the maximum instantaneous value of lift coefficient is 1.31 and differs by 3% from Hart et al. The maximum angle of attack for case 2 is  $22^\circ$  and occurs at  $t/T = 0.25$ . This value of  $C_L$  is much greater than the static value at the same effective angle of attack and clearly shows the benefit of unsteady effects.

Looking at the horizontal force, cases 1 and 2 have a drag value of 0.0526 and 0.0742. Even though, the numbers look comparable, case 2 actually produces about 30% higher drag compared to case 1. Case 2 also has larger maximum instantaneous drag. Clearly, the use of pitching motion along with the plunge motion is helping in reducing the average drag without altering the lift significantly.

Figures 15, 16 compare the velocity contour (normalized by the freestream velocity) at  $3/4^{th}$  span from the current simulation with experimental results for the respective cases. Even though there are some differences in the magnitude, overall there is a good correlation between the PIV data of Hart et al. (Ref. 8) and the current results. As expected, both the cases show separation during the mid-stroke due to the higher instantaneous effective angles seen during this period. For the same reason,

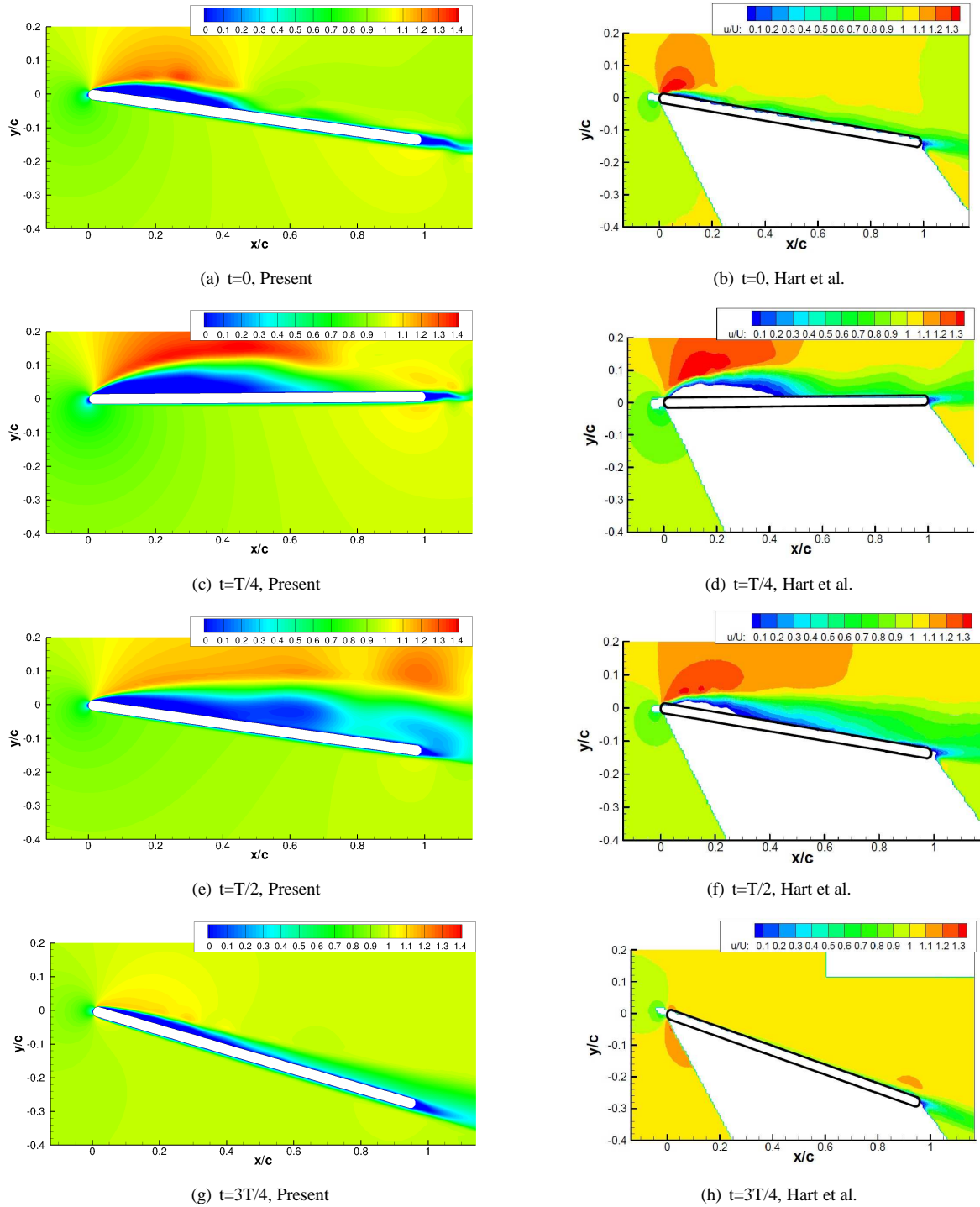


Figure 15: Velocity Contours for Case 1 at  $3/4^{th}$  span, 3D flat plate

case 2 shows larger separation when compared to case 1. Further, it can be seen from these plots, that the leading edge vortex for both the cases almost always sits in a position such that the force generated by its low pressure is vectored in the drag direction. This is consistent with

what was seen before while looking at the instantaneous forces. In addition, this suggests that it might be possible to produce thrust instead of drag for the same flow conditions by choosing the kinematics appropriately. One possibility would be to have a kinematics such that the

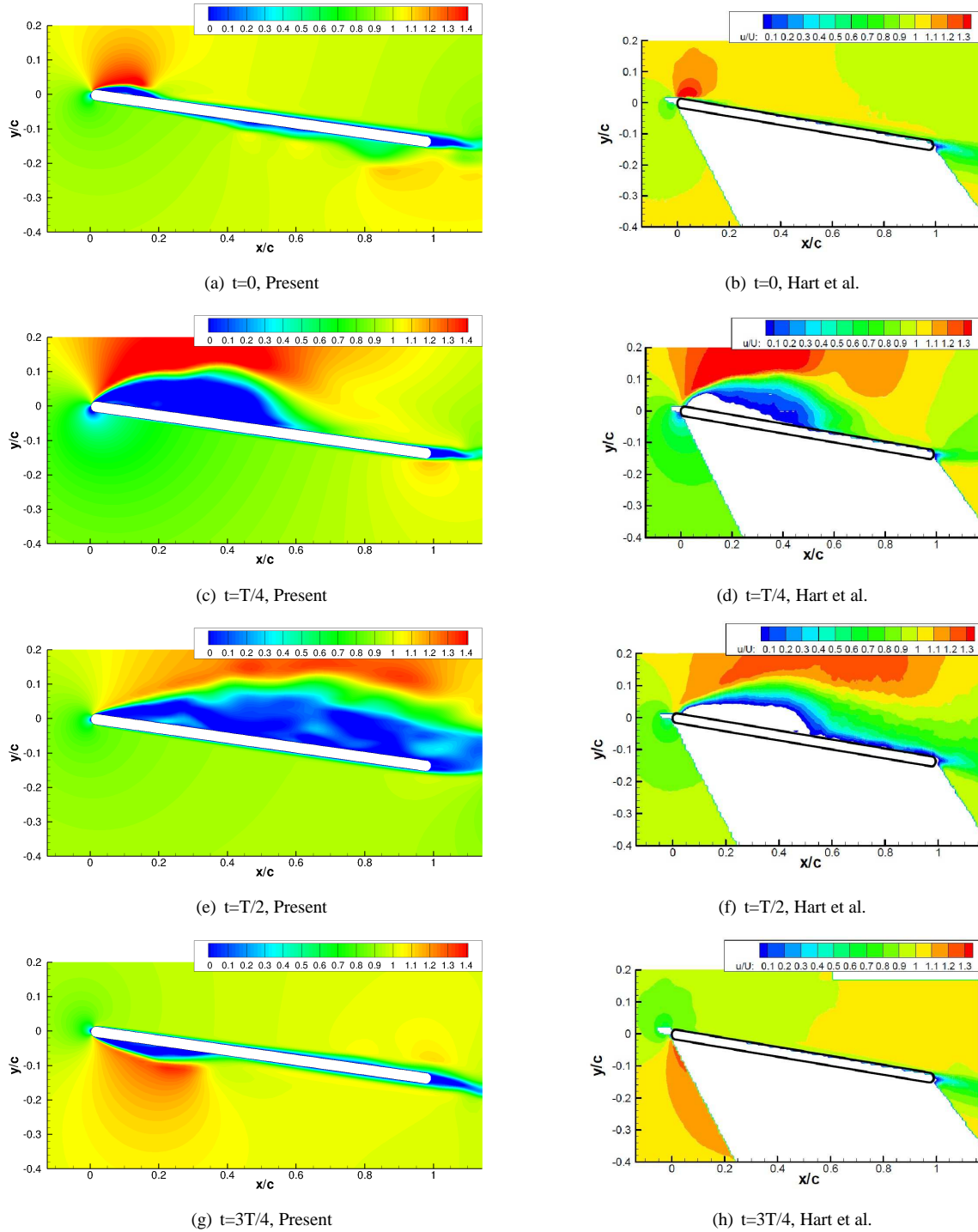


Figure 16: Velocity Contours for Case 2 at  $3/4^{th}$  span, 3D flat plate

wing is pitched in the opposite direction as compared to the effective angle seen by it due to the combined pitch and plunge motion during the mid-stroke. The leading edge vortex could thus be positioned to produce thrust. Such a kinematics is used in the next case studied.

### Root based flapping (NACA 0005)

The second type of motion considered here is a root flapping wing. A spanwise tapered wing with NACA 0005 airfoil cross section which was experimentally studied by

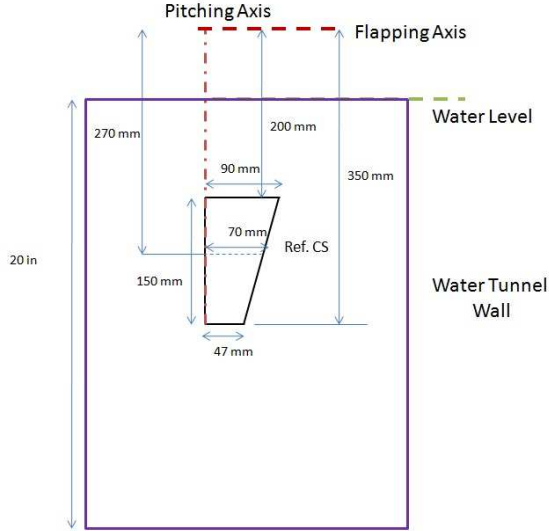


Figure 17: Wing geometry for Yuan root flap case

Yuan et al. (Ref. 10) at the National Research Council (NRC), Canada in a water tunnel, is simulated here. The water tunnel had a 15 in (width)  $\times$  20 in (height) test section. The wing geometry is shown in Fig. 17. It has a span of 0.35m, root chord of 0.09m and tip chord of 0.07m. The reference section is chosen at a spanwise position of 0.25m and has a chord of 0.07m. The flap kinematics are as follows:

$$\begin{aligned}\gamma &= \gamma_o \cos(2 \cdot \pi f \cdot t), \\ \theta &= -\theta_a \sin(2 \cdot \pi f \cdot t)\end{aligned}$$

with  $\gamma_o = 15^\circ$  and  $\theta_a = 40^\circ$ . The flapping frequency is 0.46Hz. The reduced frequency at the reference section is 1.6, based on reference chord and maximum tip velocity. The wing is pitched about the leading edge. The freestream velocity is 0.0635 m/s and the maximum tip velocity is 0.264m/s. The reference velocity with which all the quantities are normalized is given by  $\sqrt{(0.0635^2 + 0.264^2)} = 0.2715\text{m/s}$ . The Reynolds number at the reference section is about 19,000 (based on the reference section chord and reference velocity). Yuan et al. also carried out 3D computations using an incompressible solver to simulate their experiments. In their simulation, the flow was assumed to be laminar. In the current work, two separate simulations are done: one assuming fully turbulent flow and the other assuming laminar flow. No significant differences are found between the results. Therefore, only results from the laminar simulation are presented here.

The simulation in the present work is done using a two mesh overset system consisting of a body-fitted curvilinear blade mesh overlaid onto a Cartesian background mesh. The blade mesh has clustering at the blade root and tip as well as leading and trailing edges. The Carte-

sian background is refined to resolve tip vortex evolution, see Figure 18. The blade mesh has 267 points in the wrap around, 101 points in the spanwise and 93 points in the normal directions. The Cartesian background mesh has 172 points in the streamwise, 183 points in the spanwise and 92 points in the vertical directions. Implicit hole-cutting method developed by Lee (Ref. 24) and refined by Lakshminarayan (Ref. 18) is used to find the connectivity information between the overset meshes. Calculations are done using 1440 iterations per flap cycle and each iteration uses 10 subiterations to remove linearization error. Note that, Yuan et al. used a grid with  $481 \times 129 \times 33$  points and used only 384 timesteps per cycle. Therefore, the current simulation has better off-surface spatial as well as time resolution when compared to Yuan et al.'s simulation. To help ensure an accurate and stable simulation, OVERTURNS is run at a Mach of 0.05 rather than the lower experimental value. Since the Mach numbers involved in these studies are well within the incompressible limit, it is expected that small variations in Mach number will not have a significant effect on the final results.

Figures 19 and 20, respectively, show the variation of lift ( $C_L$ ) and drag ( $C_D$ ) coefficients with time. Note that, the lift and drag coefficients were obtained by normalizing with the wing planform area and the reference velocity (described earlier). As it can be seen in the figure, the current results correlate well with the numerical results of Yuan et al. When both the computational results are compared with the experimental data, there is satisfactory agreement between the results. However, there are some differences in the computed magnitude of the secondary peak found in the lift time history when compared to that in the experimental data. In addition, while both the computations predict zero net lift over a flap cycle, the experimental data show a small positive value due to dissimilar peaks obtained during upstroke and downstroke. Note that some of these differences are reflected even in the drag time history. The reason for these differences between the computational and the experimental results is not clear at this point. Yuan et al. had mentioned that the differences could possibly be because the water wall effects in the simulation were ignored. However, a simulation with the inclusion of wall effects in the current study did not result in any significant change in the lift and drag time histories.

Looking at the variation of drag with time, we can see that it has a negative value at all times, thus producing a net thrust over a flap cycle. The net drag coefficient predicted from the current simulation is  $-0.3793$  and it lies within 10% of the experimental value. Clearly, the kinematics used in this case helps in producing thrust as opposed to the earlier case of Hart et al. (Ref. 8). To understand the reason for the thrust production, the vari-

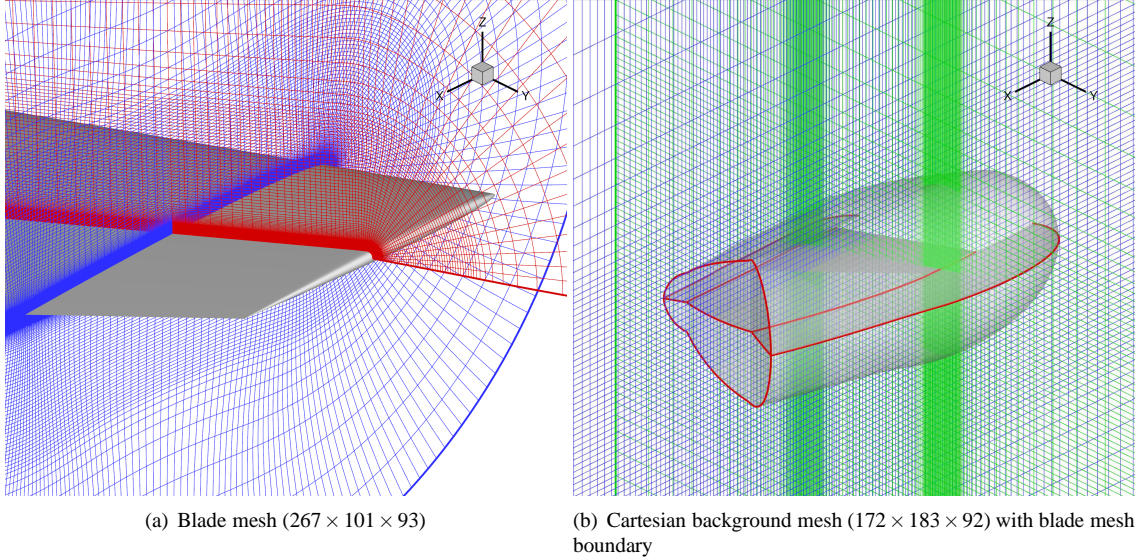


Figure 18: Computational mesh for 3D root flapping wing simulation.

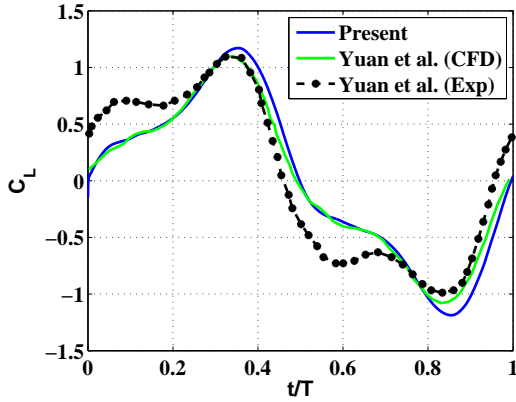


Figure 19:  $C_L$  variation with time for 3D root flapping case.

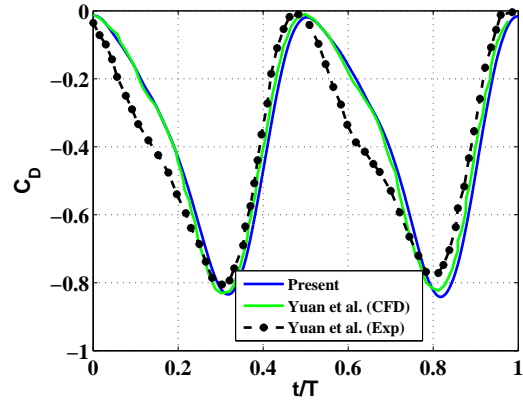


Figure 20:  $C_D$  variation with time for 3D root flapping case

ation of pitch angle along with the effective angle of attack seen by the reference section of the wing is plotted over a flap cycle, see Fig. 21. The effective angle of attack is obtained by adding the angle of attack due to the wing pitch and that due to the flapping motion. The wing pitch angle follows the prescribed sinusoidal motion with  $40^\circ$  amplitude. The effective angle of attack, on the other hand, stays relatively constant over the middle part of the stroke and at all times it has a sign opposite to that of the wing pitch. As a result, the leading edge vortex is always formed on the surface (upper or lower) of the wing that is facing the thrusting direction, thus vectoring the force in the forward direction. The low pressure created by the leading edge vortex is shown in Fig. 22, where the pressure coefficient (normalized by reference veloc-

ity) contours at the reference section are plotted at different instances in time as the wing moves from the topmost position to the bottommost position. The contour plots obtained from the current simulation are compared with those obtained by Yuan et al. (Ref. 10) as a part of validation. Thus, it can be clearly seen that by optimizing flapping kinematics, the lift and thrust can be tailored for application to MAVs. Figures 23 and 24, respectively, show the pressure contour plots at spanwise locations that are at 10% and 90% wing span location (from the root). Again, the presence of leading edge vortices are identified through mid portion of the wing stroke, but the strength of the vortex is slightly different at various sections. Note that, the current simulation preserves the vortices better when compared to the simulation of Yuan et al., due to

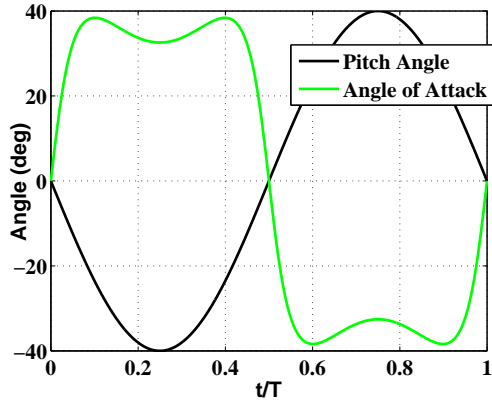


Figure 21: Variation of pitch angle and effective angle of attack at reference section for 3D root flapping case.

better off-surface grid as well as time resolution used in the present study.

A 2D simulation, which mimicked the motion of the reference section of the current case, was done earlier. Comparing to the 2D results shown earlier in Fig. 11, it can be seen that the vortices in 3D are smaller and dissipate into the flow quickly (also as observed by Yuan et. al). Due to this, the maximum lift and thrust produced in the 3D case is lower. Thus, 3D effects are seen to significantly alter the lift and drag for a flapping wing MAV.

A good flow visualization can be obtained by looking at the iso-surfaces of the so-called  $q$ -criterion (Ref. 25) colored with vorticity contour, as shown in Fig. 25. The  $q$ -criterion, which is the second invariant of the velocity gradient tensor, extracts the rotational flow regions without including the highly strained regions, such that vortical regions are highlighted. As a result, leading edge vortex along with the root and tip vortices can be easily identified in Fig. 25. The plot clearly shows the three-dimensionality of the flow-field. While the leading edge vortex is seen to be formed throughout the mid-sections of the wing, it is absent near the root and tip regions. At the root and tip, the flow feature is dominated by the root and tip vortices, respectively. All the vortices stay attached to the wing during the middle of the stroke, but are seen to get detached when the wing flips over.

### Summary and Conclusions

A compressible RANS solver was used to simulate the aerodynamics of a flapping wing MAV. The analysis was first validated in 2D flow cases and showed good correlation for all the cases considered. The first case was at relatively high Reynolds numbers for MAV applications. It was observed that thrust increases with plunging frequency due to the increasing suction of the leading edge

vortex. As long as this vortex is ahead of the position of maximum thickness, it results in the production of a propulsive force. However, if this vortex convects aft, thrust drops.

Validation was then carried out for combined pitch and plunge motions at high Reynolds numbers. It was observed that the thrust produced was higher for this case as compared to pure plunge. The mechanism of thrust production was again the suction force due to formation of leading edge vortex. But in this case, the vectoring of the chordwise force is determined by combination of pitch angle and the position of the vortex. For the flapping wing to produce thrust, the vortex may be positioned on the top or bottom of the airfoil (which depends on the angle of attack), but the suction force should be vectored in the propulsive direction (which depends on the pitch angle and the phasing between pitch and plunge). Good correlation was achieved for both the cases.

Simulation was then carried out for a low Reynolds number case, which is applicable to MAVs. It should be noted that all the 2D cases were symmetric in upstroke and downstroke and hence the average lift was zero. For this case, the instantaneous lift and drag values were also validated. Very high value of maximum instantaneous lift coefficient was observed which was much greater than the corresponding static lift coefficient at the same effective angle of attack. This clearly shows the beneficial effect of unsteadiness on the aerodynamics.

3D validation was then carried out for two configurations. The first configuration was a heaving and pitching flat plate wing with low aspect ratio. Validation of instantaneous forces and flow fields was carried out with experimental data and PIV results. Two cases were considered, pure plunge at fixed positive angle and a case with pitching modulation over a constant pitch angle. Due to an asymmetry in the kinematics, an average lift was produced in both the cases. However, the kinematics was such that the wing produced drag almost throughout the entire cycle for both the cases.

The second configuration was root based flapping which is more representative of natural flyers. A span-wise tapered wing was simulated in pitch and flap. Good correlation of instantaneous forces and flow fields was seen with prior work. The flowfield was highly three dimensional with the flow dominated by leading edge vortices in the midsection but by the root and tip vortices near the ends of the wing. Unlike the flat plate case considered before, high thrust was produced as a result of the tailoring of pitch and plunge angles and flapping frequency.

As a concluding remark, the current work demonstrates the capability of a CFD solver to characterize the flowfield of a flapping wing MAV in 3D. Future work will include looking at the various parameters like the

wing geometry and flapping kinematics which can be optimized to design a flapping wing MAV.

### Acknowledgement

This research was supported by the Armys MAST CTA Center for Microsystem Mechanics with Dr. Joseph Mait (ARL) as Technical Monitor.

### References

- <sup>1</sup>Chopra, I., "Hovering Micro Air Vehicles: Challenges and Opportunities" Proceedings AHS International Meeting on Advanced Rotorcraft Technology and Safety Operations (Heli Japan), Ohmiya, Japan, November 2010.
- <sup>2</sup>Knoller, R., "Die Gesetze des Luftwiderstandes," Flug- und Motortechnik (Wien), Vol. 3, (21), 1909, pp. 1-7.
- <sup>3</sup>Betz, A., "Ein Beitrag zur Erklarung des Segelfluges," Zeitschrift fur Flugtechnik und Motorluftschiffahrt, Vol. 3, 1912, pp. 269-272.
- <sup>4</sup>Katzmayr, R., "Effect of Periodic Changes of Angle of Attack on Behavior of Airfoils," NACA TM 147, Oct. 1922.
- <sup>5</sup>McCroskey, W.J., "Unsteady Airfoils", *Annual Review Fluid Mechanics*, Vol. 14, 1982, pp. 285-311.
- <sup>6</sup>Carr, L., "Progress in Analysis and Prediction of Dynamic Stall," *Journal of Aircraft*, Vol. 25, 1988, pp. 6-17.
- <sup>7</sup>Anderson, J. M., Streitlin, K., Barrett, D. S., and Triantafyllou, M. S., "Oscillating Foils of High Propulsive Efficiency," *Journal of Fluid Mechanics*, Vol. 360, 1998, pp. 41-72.
- <sup>8</sup>Hart, A. and Ukeiley, L., "Low Reynolds Number Unsteady Aerodynamics over a Pitching-Plunging Flat Plate," AIAA Paper 2010-387, January 2010.
- <sup>9</sup>Malhan, R., Benedict, M., Chopra, I., "Experimental Investigation of a Flapping Wing Concept in Hover and Forward Flight for Micro Air Vehicle Applications," Proceedings of the 66th Annual American Helicopter Society Forum, Phoenix, Az, May 11-14, 2010.
- <sup>10</sup>Yuan, W., Lee, R., Hoogkamp, E., and Khalid, M., "Numerical and Experimental Simulations of Flapping Wings," *International Journal of Micro Air Vehicles*, Vol. 2, (3), September 2010, pp. 181-209.
- <sup>11</sup>Tuncer, I. H., and Platzer, M. F., "Thrust Generation Due to Airfoil Flapping," *AIAA Journal*, Vol. 34, (2), Feb. 1996, pp. 324-331.
- <sup>12</sup>Tuncer, I. H., Walz, R., and Platzer, M. F., "A Computational Study of the Dynamic Stall of a Flapping Airfoil," AIAA Paper 98-2519, June 1998.
- <sup>13</sup>Isogai, K., Shinmoto, Y., and Watanabe, Y., "Effects of Dynamic Stall on Propulsive Efficiency and Thrust of Flapping Airfoil," *AIAA Journal*, Vol. 37, (10), Oct. 1999, pp. 1145-1151.
- <sup>14</sup>Young, J., and Lai, J. C. S., "Mechanisms Influencing the Efficiency of Oscillating Airfoil Propulsion," *AIAA Journal*, Vol. 45, (7), July 2007, pp. 1695-1702.
- <sup>15</sup>RTO Technical Report, "Unsteady Aerodynamics of Micro Air Vehicles," Final Report of Task Group AVT-149, September 2010.
- <sup>16</sup>Lakshminarayan, V. K., and Baeder, J. D., "Computational Investigation of Micro Hovering Rotor Aerodynamics," *Journal of the American Helicopter Society*, Vol. 55, (2), April 2010.
- <sup>17</sup>Lakshminarayan, V. K., and Baeder, J. D., "Computational Investigation of Micro-Scale Coaxial Rotor Aerodynamics in Hover," *Journal of Aircraft*, Vol. 47, (3), June 2010, pp. 940-955.
- <sup>18</sup>Lakshminarayan, V. K., "Computational Investigation of Micro-Scale Coaxial Rotor Aerodynamics in Hover," *Ph.D. Dissertation*, Department of Aerospace Engineering, University of Maryland at College Park, 2009.
- <sup>19</sup>Pulliam, T., and Chaussee, D., "A Diagonal Form of an Implicit Approximate Factorization Algorithm," *Journal of Computational Physics*, Vol. 39, (2), February 1981, pp. 347-363.
- <sup>20</sup>Buelow P. E. O., Schwer D. A., Feng J., and Merkle C. L., "A Preconditioned Dual-Time, Diagonalized ADI scheme for Unsteady Computations," AIAA paper 1997-2101, 13th AIAA Computational Fluid Dynamics Conference, Snowmass Village, CO, June 29-July 2, 1997.
- <sup>21</sup>Pandya, S. A., Venkateswaran, S., and Pulliam, T. H., "Implementation of Preconditioned Dual-Time Procedures in OVERFLOW," AIAA paper 2003-0072, 41st AIAA Aerospace Sciences Meeting and Exhibit, Reno, NV, January 6-9, 2003.
- <sup>22</sup>Spalart, P.R., and Allmaras, S.R., "A One-equation Turbulence Model for Aerodynamic Flows," AIAA Paper 1992-0439, 30th AIAA Aerospace Sciences Meeting and Exhibit, Reno, NV, January 6-9, 1992.
- <sup>23</sup>Menter, F.R., "Two-Equation Eddy-Viscosity Turbulence Models for Engineering Application," *AIAA Journal*, Vol. 32, 1994, pp. 269-289.

<sup>24</sup>Lee, Y. "On OversetGrid Connectivity and Automated Vortex Tracking in Rotorcraft," *Ph.D Dissertation*, Department of Aerospace Engineering, University of Maryland at College Park, 2008.

<sup>25</sup>Jeong, J. and Hussain, F., "On the Identification of a Vortex," *Journal of Fluid Mechanics*, Vol. 285, 1995, pp.69-94.

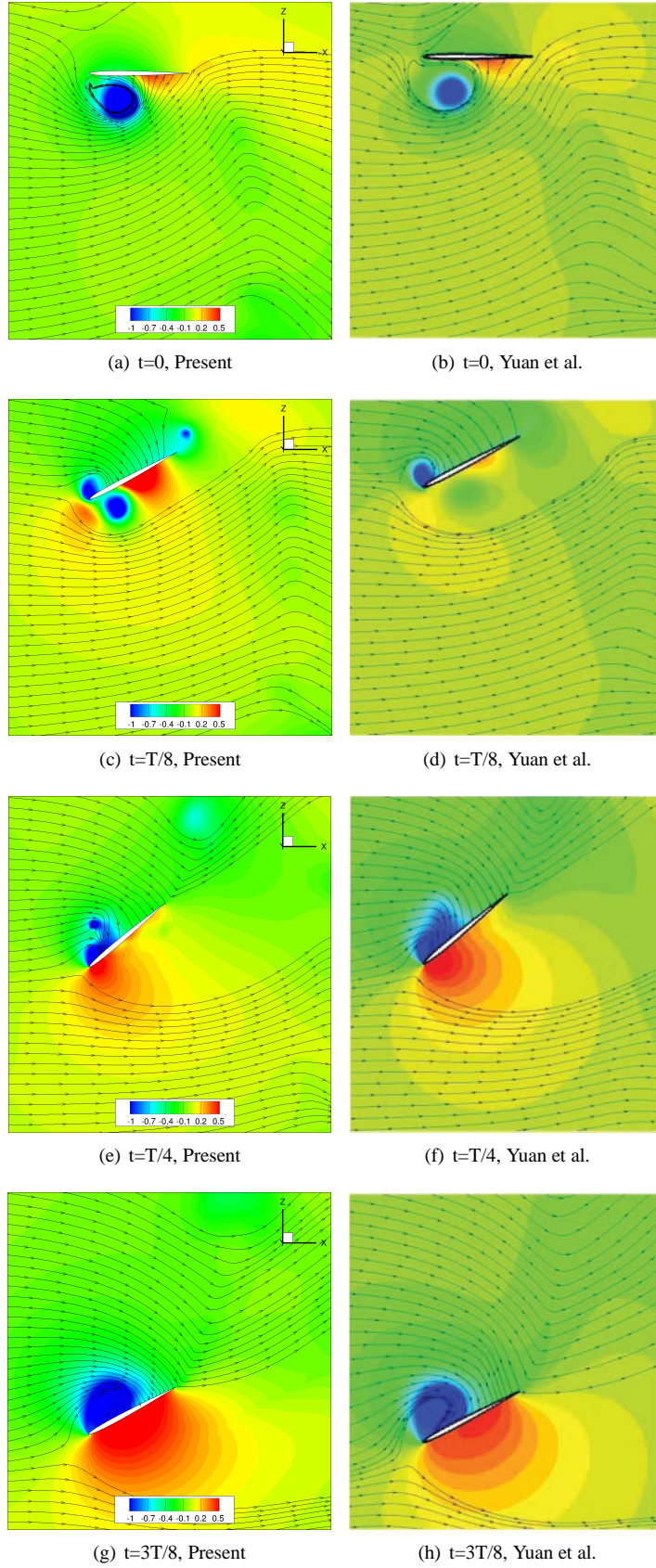


Figure 22: Pressure contours at reference section for 3D root flapping case.

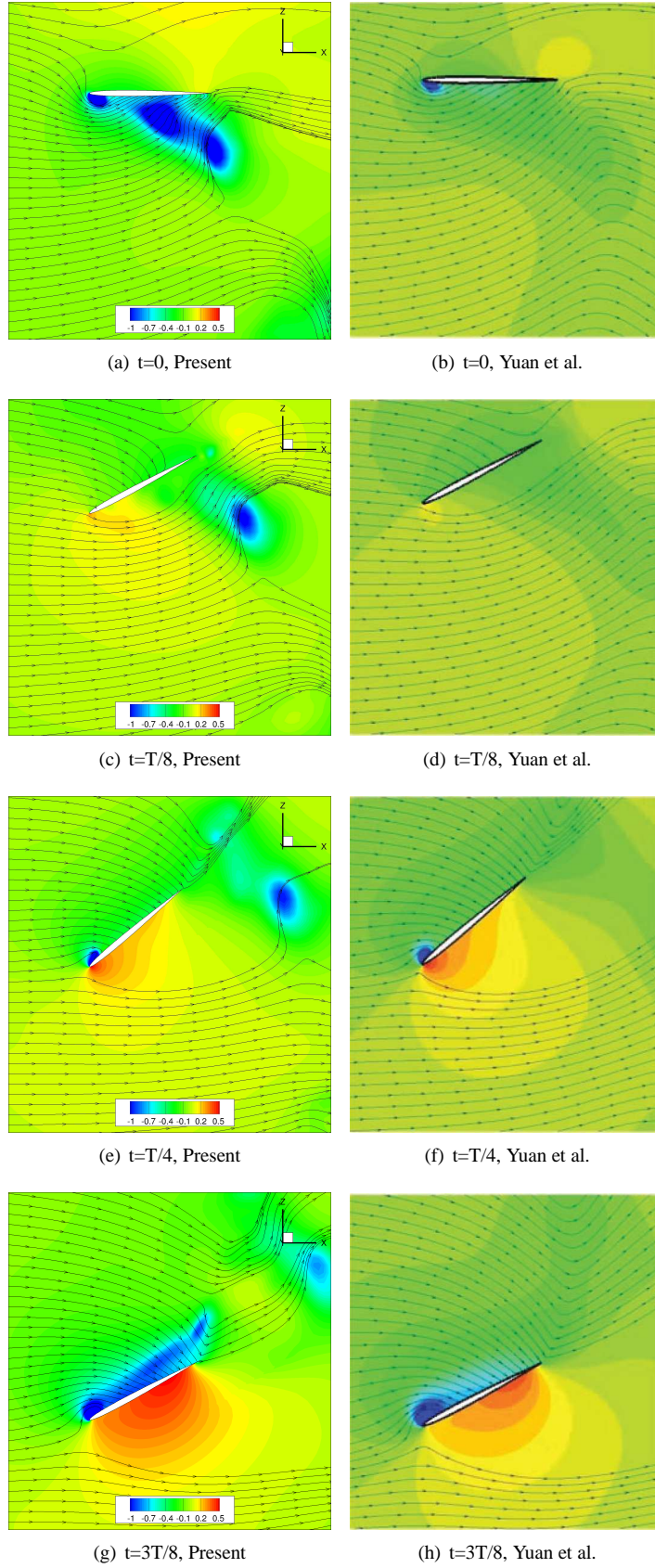


Figure 23: Pressure contours at 10% wing span location for 3D root flapping case.

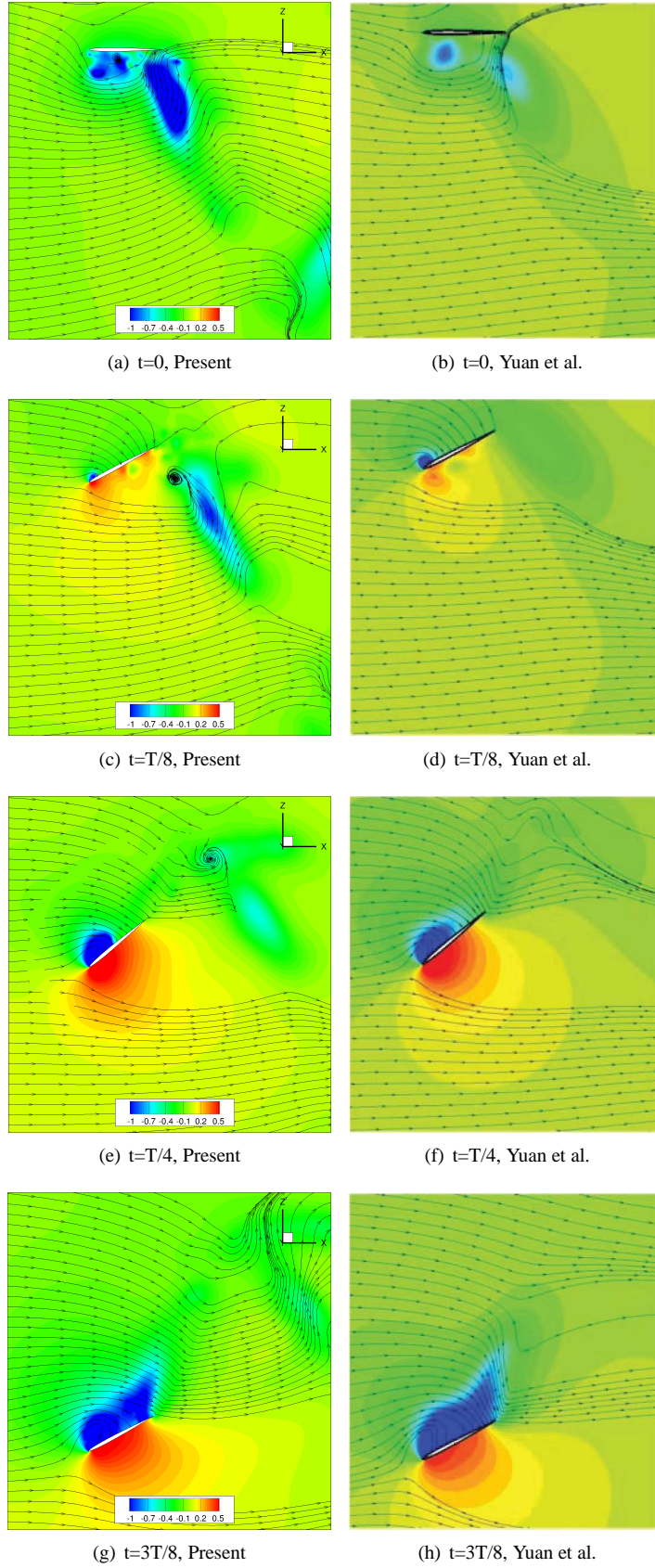


Figure 24: Pressure contours at 90% wing span location for 3D root flapping case.

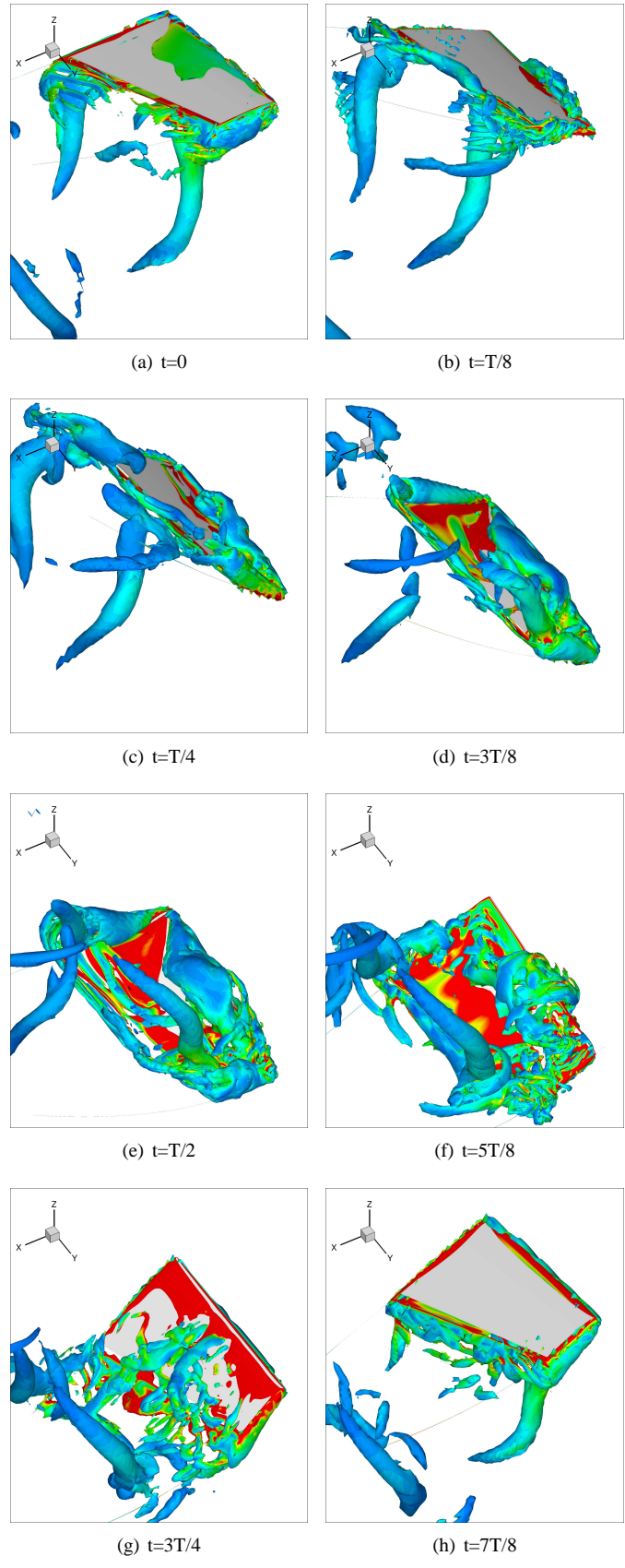


Figure 25: Iso-surfaces of second invariant of the velocity gradient tensor colored with azimuthal vorticity contour from 3D root flapping simulation.